Magnetic properties, microstructure, composition, and morphology of greigite nanocrystals in magnetotactic bacteria from electron holography and tomography

Takeshi Kasama,[1,2] **Mihály Pósfai,**[3,*] **Ryan K.K. Chong,**[2] **Anna P. Finlayson,**[2] **Peter R. Buseck,**[4] **Richard B. Frankel,**[5] **and Rafal E. Dunin-Borkowski**[2,1]

[1]Frontier Research System, The Institute of Physical and Chemical Research, Japan
[2]Department of Materials Science and Metallurgy, University of Cambridge, U.K.
[3]Department of Earth and Environmental Sciences, Pannon University, Veszprém, Hungary
[4]Department of Geological Sciences, Arizona State University, Tempe, Arizona, U.S.A.
[5]Department of Physics, California Polytechnic State University, San Luis Obispo, California, U.S.A.

Abstract

Magnetotactic bacteria comprise several aquatic species that orient and migrate along geomagnetic field lines. This behavior is based on the presence of intracellular ferrimagnetic grains of the minerals magnetite (Fe_3O_4) or greigite (Fe_3S_4). Whereas the structural and magnetic properties of magnetite magnetosomes have been studied extensively, the properties of greigite magnetosomes are less well known. Here we present a study of the magnetic microstructures, chemical compositions, and three-dimensional morphologies and positions of Fe-sulfide crystals in air-dried cells of magnetotactic bacteria. Data were obtained using several transmission electron microscopy techniques that include electron holography, energy-filtered imaging, electron tomography, selected-area electron diffraction, and high-resolution imaging. The studied rod-shaped cells typically contain multiple chains of greigite magnetosomes that have random shapes and orientations. Many of the greigite crystals appear to be only weakly magnetic, because the direction of their magnetic induction is almost parallel to the electron beam. Nevertheless, the magnetosomes collectively comprise a permanent magnetic dipole moment that is sufficient for magnetotaxis. One of the cells, which is imaged at the point of dividing, contains multiple chains of both equidimensional Fe-sulfide and elongated Fe-oxide crystals. The equidimensional and elongated crystals have magnetic properties that are consistent with those of greigite and magnetite, respectively. These results can be useful for obtaining a better understanding of the function of magnetotaxis in sulfide-producing cells, and they have implications for the interpretation of the paleomagnetic signals of greigite-bearing sedimentary rocks.

Keywords: Greigite, magnetotactic bacteria, transmission electron microscopy, electron holography, electron tomography, magnetic properties, biomineralization

Introduction

Iron-sulfide magnetosomes in magnetotactic bacteria were first described in 1990 (Farina et al. 1990; Mann et al. 1990). The primary mineral in the magnetosomes was identified as greigite (Fe_3S_4) (Heywood et al. 1990, 1991; Bazylinski et al. 1990, 1993), which is ferrimagnetic and isostructural with magnetite (Fe_3O_4). In subsequent studies, the structures and compositions of sulfide magnetosomes were analyzed in detail, and non-magnetic precursors of greigite (primarily mackinawite, FeS) also were identified (Pósfai et al. 1998a, 1998b). Despite these studies, sulfide-producing magnetotactic bacteria remain enigmatic because they are not available in pure culture (Bazylinski and Frankel 2004). Whereas the magnetic properties of magnetite magnetosomes have been studied from many perspectives for several bacterial strains (Diaz-Ricci et al. 1991; Moskowitz et al. 1993; Proksch et al. 1995; Dunin-Borkowski et al. 1998, 2001; McCartney et al. 2001; Weiss et al. 2004; Simpson et al. 2005), little is known about the magnetic microstructure of

sulfide magnetosomes (Diaz-Ricci and Kirschvink 1992). The magnetic parameters of greigite, including the critical particle size for single-domain behavior, and the effects of shape and magnetocrystalline anisotropy on magnetic microstructure, are not known satisfactorily (Hoffmann 1992; Roberts 1995; Dekkers et al. 2000; Peters and Dekkers 2003; Chen et al. 2005). In the present study, we characterize Fe-sulfide magnetosomes comprehensively, with the aim of providing measurements that may shed light on sulfide biomineralization processes and on the biological functions of sulfide magnetosomes, as well as on the contribution of biogenic greigite to the paleomagnetic signal in sedimentary deposits.

Off-axis electron holography is a transmission electron microscopy (TEM) technique that can be used to study the magnetic microstructures of nanocrystals (Dunin-Borkowski et al. 2004). The method has been applied successfully to studies of magnetite magnetosomes, and it has been extremely useful for assessing the competing effects of shape and magnetocrystalline anisotropy and interparticle interactions on the magnetic properties of linear chains of magnetosomes (Dunin-Borkowski et al. 1998,

* E-mail: posfaim@almos.vein.hu

2001; McCartney et al. 2001; Simpson et al. 2005). Here we use electron holography to characterize the magnetic properties of Fe-sulfide magnetosomes quantitatively.

Accurate knowledge of the three-dimensional shapes, positions, and orientations of magnetosomes is important for interpreting their magnetic properties. However, the measurement of nanoparticle shapes is challenging (Buseck et al. 2001; van Poppel et al. 2005). In the present study, we use ultra-high-tilt series of high-angle annular dark-field (HAADF) images to provide tomographic reconstructions of three-dimensional particle shapes, orientations, and positions. Because HAADF images are affected by diffraction contrast less strongly than bright-field images, they are better suited for tomographic reconstruction of crystalline specimens (Midgley et al. 2001). We present three-dimensional reconstructions of the same magnetosomes from which electron holograms were obtained, and correlate the particle shapes and structures with their magnetic properties.

EXPERIMENTAL METHODS

Sediment and water samples containing magnetotactic bacteria were collected at Morro Bay, California in the spring of 2002. Drops were enriched in magnetotactic cells by using a bar magnet and placed on nickel TEM grids. No fixation was used, with the cells simply allowed to dry on the grids. Although this procedure may introduce artifacts, such as a flattening of the magnetosome chain and changes in the orientations of the magnetosomes, the magnetosome chains appeared to remain relatively intact. High-resolution transmission electron microscope (HRTEM) images and selected-area electron diffraction (SAED) patterns were obtained from individual crystals using JEOL 4000EX electron microscopes (at Arizona State University in 2002 and at Cambridge in 2005), operated at an accelerating voltage of 400 kV. SAED patterns were also obtained using a JEOL 3010 TEM (at Budapest in 2005).

Chemical maps and electron holograms were obtained at 300 kV using a Philips CM300-ST field-emission-gun TEM equipped with a Gatan Imaging Filter (GIF) (at Cambridge in 2002 and 2004). Additional chemical maps were obtained from bacteria that had been collected earlier (in 1998) at Sweet Springs Nature Preserve, Massachusetts, and prepared in the same way as described above. These maps were obtained at 300 kV using a JEOL 3000F TEM fitted with a field-emission gun and a GIF (at Oxford in 1999). "Jump-ratio" images were obtained by dividing two images that had been acquired using electrons that had suffered energy losses just above and below a core-loss edge in the energy-loss spectrum arising from the element of interest. These maps may contain artifacts, such as a contribution from a large, non-specific background intensity to the signal, and are used primarily for obtaining qualitative information about element concentrations. More accurate compositional maps were obtained by using three-window, background-subtracted imaging. This technique involves the acquisition of two energy-loss images below and one above the edge of interest; a power-law background modeled on the basis of the two pre-edge images is then subtracted from the post-edge image (Egerton 1986).

We used off-axis electron holography in the TEM to study the magnetic microstructures of chains and individual magnetosomes. The technique involves the use of a coherent electron source (a field-emission gun), a Lorentz lens for imaging samples in magnetic-field-free conditions, and a positively charged wire (an electron biprism), in place of one of the selected-area apertures. Part of the electron wave that travels through the region of interest on the sample is overlapped with part that travels only through vacuum by the biprism, resulting in the formation of an interference fringe pattern. The part of the electron wave that passes through the sample experiences a phase shift with respect to the part that passes through vacuum. This phase shift, which is sensitive to electric and magnetic fields in the specimen, is recorded in the spacings of the holographic fringes. By processing the recorded holograms digitally, it is possible to separate the mean inner potential (MIP) and magnetic contributions to the holographic phase shift. Details of this procedure are described by Dunin-Borkowski et al. (2004).

Ultra-high-tilt series of HAADF images for electron tomography were obtained at 200 kV using a Tecnai F20 field-emission-gun TEM (at Cambridge in 2004). HAADF images were acquired at 2° tilt intervals over a tilt range of −79° to +78° and used for three-dimensional tomographic reconstruction of the shapes of the cell and the magnetosomes. The field of view of each original image was 4383 nm. Each image was acquired for 40 s, which corresponds to 3.8×10^{-5} s dwell time per pixel.

RESULTS

Most cells are rod-shaped, with a single polar flagellum and multiple chains of Fe-sulfide magnetosomes (Fig. 1). The chains are not as well organized as is typical of magnetite-bearing bacteria. For example, many cells contain crystals that are offset from the chains and apparently scattered throughout the cytoplasm. In some cells, there are no recognizable chains, and the magnetosomes form disordered clusters (Fig. 1c). It is possible that some of the disorder of the magnetosomes is an artifact arising from air-drying of the cells. However, Keim et al. (2004a, 2004b) also observed disordered sulfide magnetosome chains in fixed cells, and we believe that most of the magnetosome orientations that we observed in the sulfide-producing cells generally reflect the original conditions. Two cells were studied in detail: the single cell shown in Figure 1d (see also Figs. 2 and 3) and a large, dividing rod (Figs. 4–12) (collected in 2002 at Morro Bay). The compositions, magnetic properties, morphologies, and structures of the Fe-sulfide magnetosomes in these two cells are described below.

Compositions measured from chemical maps

The cell shown in Figure 1d contains a double chain of magnetosomes, which are each ~60 nm in size. Figure 2 shows four chemical maps obtained from the same cell. The magnetosomes exhibit dark contrast in the C map (Fig. 2a) because the projected concentration of C is lower at their positions than elsewhere in the cell. Only a few crystals exhibit strong contrast in the O map (Fig. 2b). None of these crystals are within the double chain of magnetosomes that runs approximately parallel to the long axis of the cell. These O-rich crystals are absent from the Fe map (Fig. 2c), but are present (marked using white arrows) in the S map (Fig. 2d).
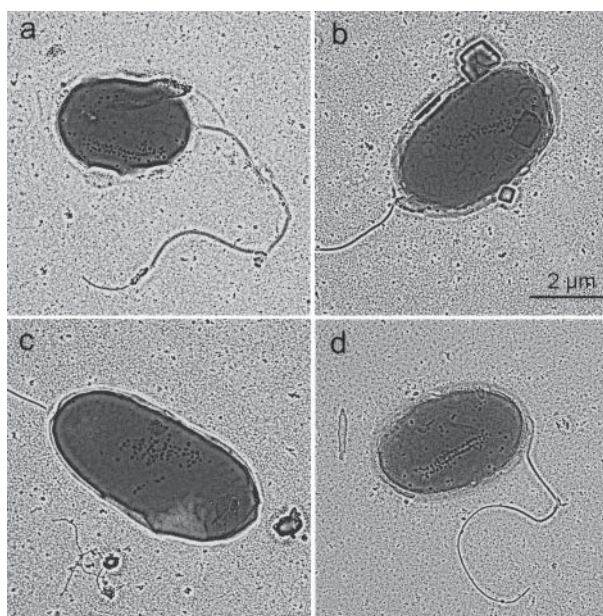
FIGURE 1. High-pass-filtered, bright-field transmission electron micrographs of rod-shaped single cells containing Fe-sulfide magnetosomes.
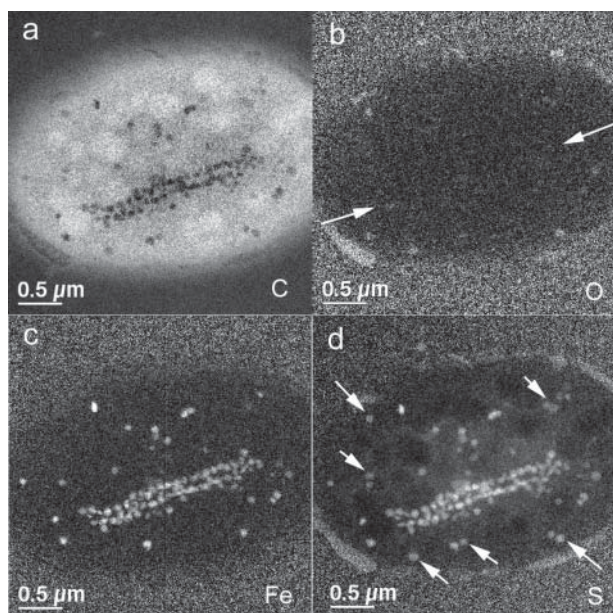
FIGURE 2. (**a**) Three-window, background-subtracted C chemical map, and (**b**) jump-ratio O, (**c**) Fe, and (**d**) S chemical maps obtained from the cell shown in Figure 1d. The white arrows mark the position of the magnetosome chain in **b**, and S- and O-bearing, Fe-free particles in **d**.

For easier visualization of variations in the compositions of the magnetosomes, a composite image in which red, green, and blue correspond to the C, S, and Fe signals, respectively, is shown in Figure 3. Light blue regions correspond to the positions of Fe sulfide crystals, whereas particles that contain S but no Fe appear green. The cell is rimmed in places by extracellular O- and S-rich material (arrowed), as indicated by the green color along the outer cell wall. Magnetic flux contours, which are superimposed onto this chemical map, are discussed below.

Figure 4 shows a magnetotactic bacterium that is apparently undergoing cell division. A multiple chain of magnetosomes, which extends along the long axis of the cell, is divided approximately equally between the two daughter cells. It is known from previous studies that the structures and compositions of Fe-sulfide magnetosomes can change in unfixed, dehydrated cells when TEM specimens are stored in air (Pósfai et al. 1998a, 1998b). Accordingly, we studied this cell more than once. Chemical maps and electron holograms were obtained both in September 2002 and in October 2004, whereas HRTEM images and SAED patterns were recorded in December 2002 and in August 2005. Electron tomography was performed on the same cell in November 2004. The multiple experiments provided an opportunity to observe compositional and magnetic changes of the magnetosomes over a period of several years.

Composite chemical and magnetic induction maps obtained
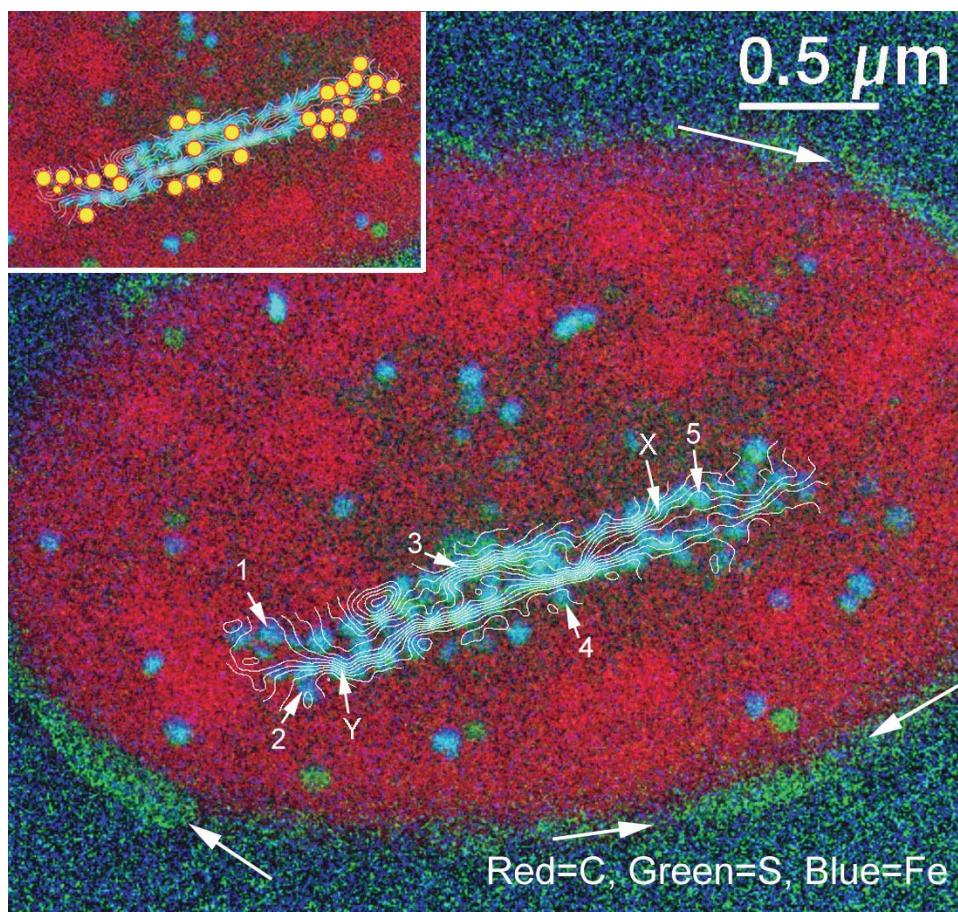
FIGURE 3. Composite image formed from three chemical maps (as indicated by the color code at the bottom of the image) and magnetic phase contours obtained using electron holography. The contour spacing is 0.075 radians. In the inset, yellow circles mark magnetosomes that appear to be either weakly magnetic or non-magnetic. Measured properties of the arrowed crystals (marked by numbers and letters) are listed in Table 1. The large arrows mark S-rich material on the cell surface.
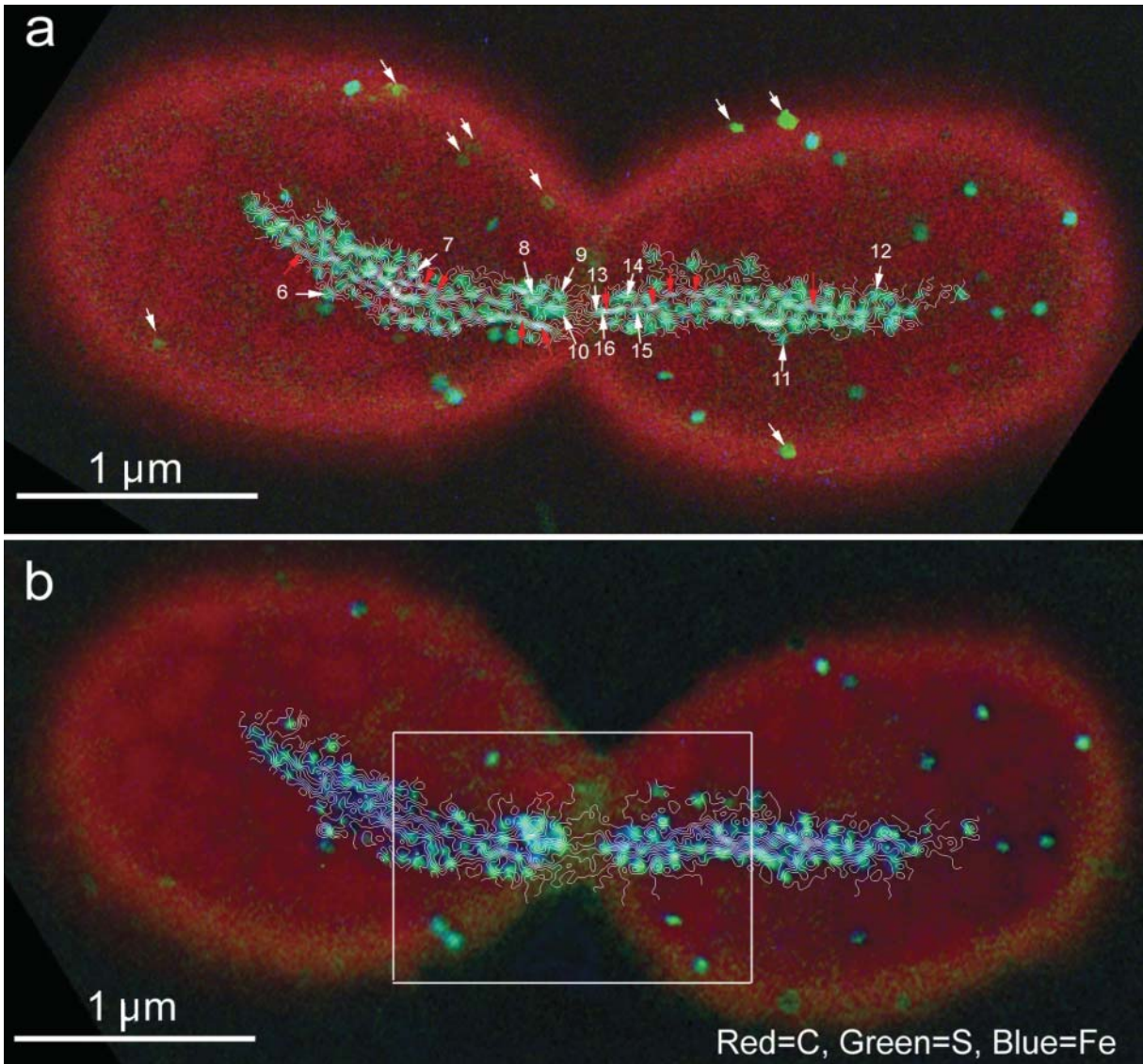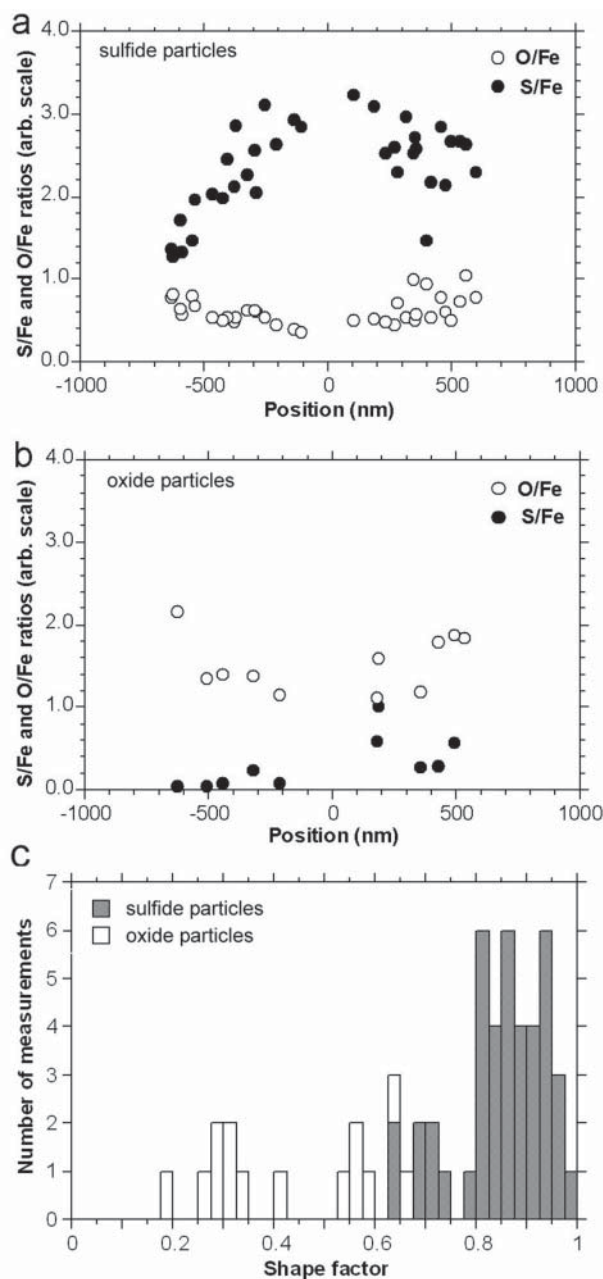
FIGURE 4. Composite images formed from chemical and magnetic induction maps acquired from a dividing cell in (**a**) September 2002 and (**b**) October 2004. The contour spacing is 0.098 radians in both images. Numbered white arrows in **a** mark crystals that are referred to in Table 2, whereas red arrows mark elongated Fe-oxide magnetosomes. White arrows without numbers point to S- and O-containing, Fe-free particles. Compositions of magnetosomes within the area boxed in **b** are shown in Figure 6.
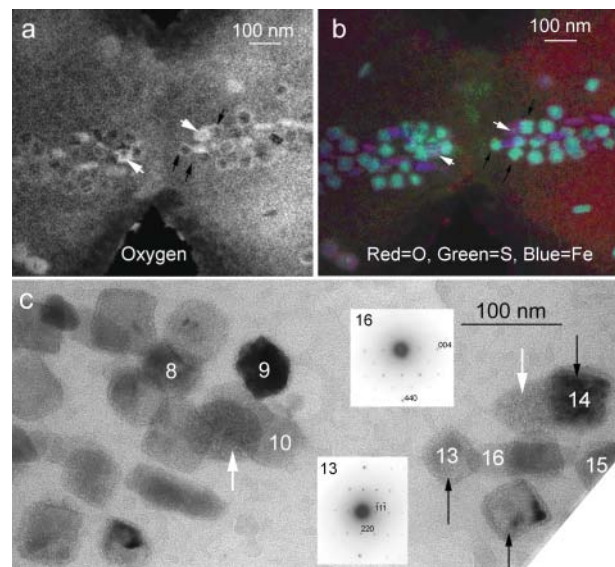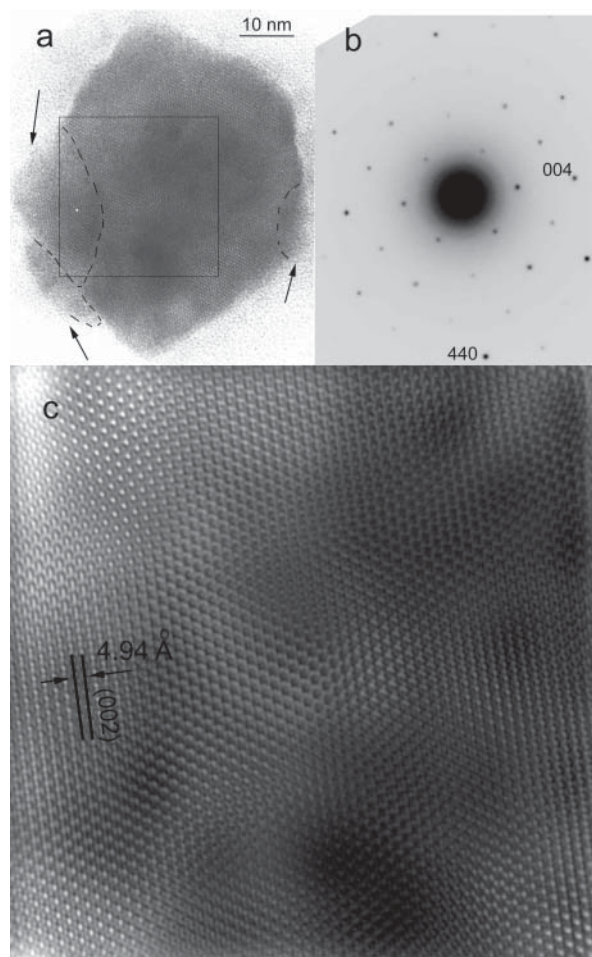

FIGURE 5. (**a**) Three-window O map, (**b**) a composite of three-window O, S, and Fe maps, and (**c**) a bright-field image of the central part of the dividing cell shown in Figure 4. SAED patterns obtained from the greigite crystal marked 13 and from the elongated magnetite crystal marked 16 are inserted in **c** in their corresponding orientations. The chemical maps and SAED patterns were obtained in 2004 and 2005, respectively. The black arrows mark greigite magnetosomes with distinct oxide shells, whereas white arrows mark thin flake-like Fe oxide particles. The same particles are arrowed in **a**, **b**, and **c**. Properties of the numbered crystals are listed in Table 2.

FIGURE 7. (a) High-resolution TEM image and (b) selected-area electron diffraction pattern obtained from crystal 9 in Figure 5 and Table 2. The arrows and dashed lines in (a) mark fragments that appear to be attached to the primary particle. (c) Fourier-filtered version of the boxed region in a. The strong contrast variations likely result from changes in crystal thickness.

FIGURE 6. (a and b) S/Fe and O/Fe ratios of particles from the boxed region in Figure 4b, plotted on the same arbitrary scale as a function of their positions within the magnetosome chain. The origin on the horizontal axis corresponds to the cell-division plane. The graphs are for (a) Fe sulfide particles and (b) Fe oxide particles. The measurements were made in 2004. (c) Shape-factor distributions of the sulfide and oxide particles shown in a and b. The shape factor of each crystal was calculated from to the formula $(a + b)/2c$, where $a \leq b \leq c$ and a, b, and c are the three axes of a best-fitting ellipsoid that was determined from HAADF images taken at 0° and 44° tilt angles.

in 2002 and 2004 are shown in Figures 4a and 4b, respectively. Jump-ratio and three-window chemical maps were used to form Figures 4a and 4b, respectively. Unfortunately, it is generally more difficult to obtain quantitative compositional information about a sample from a jump-ratio image than from a three-window elemental map, and Fe/S ratios such as those shown in Figures 4a and 4b cannot be compared with each other directly. Nevertheless, it is apparent that the magnetosome chain has a light green color in Figure 4a, indicating that most particles contain Fe and S. The distribution of red color in Figure 4a shows that the projected concentration of C is higher along the thick cell wall than in the interior of the cell. The new cell membrane that is forming in the gap between the two halves of the chain is enriched in O and S (Figs. 5a and 5b) but not in C (not shown). As in the single cell shown in Figure 2, magnetosome-sized crystals that contain S and O but not Fe also occur in the cell.

Even though the compositions in Figures 4a and 4b cannot be compared directly for the reasons discussed above, some changes over the two-year period are apparent. There is more variation in color within the multiple magnetosome chain in Figure 4b than in Figure 4a, suggesting that the compositions of the magnetosomes changed variably, depending on their positions in the

chain. The predominantly blue color of the crystals in Figure 4b may indicate that many of the Fe-sulfide magnetosomes have converted partially to Fe-oxide. The S-rich granules that were near the edges of the cell are now either absent or exhibit a much fainter S signal in Figure 4b than in Figure 4a.

A detailed analysis of the compositions of individual magnetosomes was performed on the O, S, and Fe three-window maps acquired in 2004. In the multiple magnetosome chain, most of

TABLE 1. Summary of observations for the magnetosomes numbered in Figure 3

Particle number and mineral species	Shape factor (width/ length)	Axis of elongation (based on SAED)	Orientation of axis of elongation with respect to chain axis	Apparent magnetic induction (T)	Other comments
1 greigite	0.83	[110] and [100]	perpendicular along [110], parallel along [100]	not detectable	L-shaped crystal in projection, probably formed from two individual crystals. Planar defect along [111].
2 greigite	0.79	[100]	perpendicular	0.02	Likely to be an aggregate of two or three crystals, resulting in uneven contrast in the center of the crystal.
3 greigite	0.72	[113]	parallel	0.13	Patchy contrast. Induction lines parallel to elongation direction and chain axis.
4 greigite	0.77	[511]	perpendicular	0.03	Offset from the chain axis. Likely to be an aggregate of several crystals.
5 greigite	0.73	not identified	perpendicular	0.04	Patchy contrast.
X not identified	1.00	–	–	0.06	Induction lines parallel to chain axis.
Y not identified	0.92	not identified	~30°	0.13	Induction lines parallel to elongation direction.

TABLE 2. Summary of observations for the magnetosomes numbered in Figure 4a

Particle number and mineral species	Shape factor (width/ length)	Axis of elongation (based on SAED)	Orientation of axis of elongation with respect to chain axis	Composition in 2002	Composition in 2004	Apparent magnetic induction in 2002	Apparent magnetic induction in 2004	Other comments
6 greigite	0.75	[110]	~45°	sulfide + oxide rim on one side	sulfide + oxide shell	medium	strong	A
7 greigite	0.82	[110]	~45°	sulfide + oxide shell	mostly oxide	strong	weak	B
8 greigite	0.70	[130]	parallel	sulfide	sulfide + minor oxide	strong	strong	C
9 greigite	0.85	[110]	~45°	sulfide	sulfide + oxide shell	medium (0.13 T)	medium (0.10 T)	D
10 greigite	0.87	not identified	[113] parallel to chain axis	sulfide + minor oxide	sulfide + oxide shell	weak (0.06 T)	medium (0.11 T)	E
11 greigite	0.93	not identified	[130] parallel to chain axis	sulfide + minor oxide	sulfide + oxide shell	weak	weak	F
12 greigite	0.70	[100]	~30°	sulfide + minor oxide	sulfide + oxide shell	weak	weak	G
13 greigite	0.95	not identified	[111] parallel to chain axis	sulfide + minor oxide	sulfide + oxide shell	strong (0.16 T)	medium (0.10 T)	H
14 greigite	0.92	not identified	[110] parallel to chain axis	sulfide + minor oxide	sulfide + oxide shell	strong (0.15 T)	weak (0.06 T)	I
15 greigite	0.86	not identified	[111] parallel to chain axis	sulfide + minor oxide	sulfide + oxide shell	strong (0.15 T)	medium (0.12 T)	J
16 magnetite	0.30	[100]	parallel	oxide	oxide	very strong (0.62 T)	very strong (0.52 T)	K

A = Possibly several flakes on top of one another. Induction lines wavy.
B = Induction lines parallel to chain axis.
C = Induction lines parallel to elongation direction and chain axis.
D = Induction lines parallel to elongation direction.
E = Induction lines parallel to chain axis.
F = Offset from the chain. Induction lines at ~45° to the chain axis.
G = Induction lines roughly parallel to elongation direction.
H = Induction lines parallel to chain axis.
I = Induction lines parallel to chain axis
J = Induction lines parallel to chain axis.
K = Induction lines parallel to elongation direction.

the particles have equidimensional, rounded shapes and contain primarily Fe and S. However, elongated, rod-shaped crystals and some flake-like particles also occur. These crystals are both morphologically and compositionally distinct from most of the particles in the chain. The elongated and flake-like particles contain little or no S, but significant O (Fig. 5a). As indicated
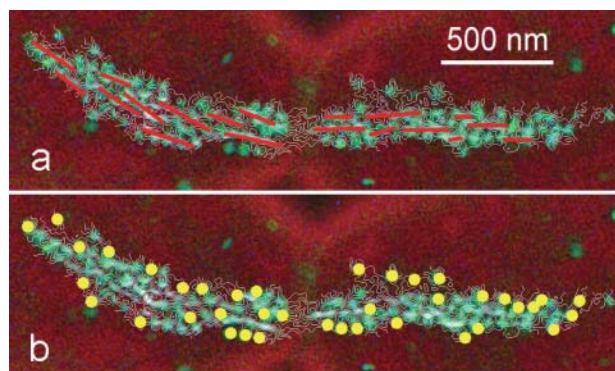

FIGURE 8. Magnetic contour map of the multiple magnetosome chain in the dividing cell shown in Figure 4a. Red lines in (**a**) mark uniformly magnetized chain segments consisting of several magnetosomes. Yellow dots in (**b**) mark crystals that appear to be either weakly magnetic or non-magnetic.

by their violet color in Figure 5b, they contain primarily Fe and O. Thus, the dividing cell contains both sulfide and oxide magnetosomes.

In addition to identifying Fe-sulfide and Fe-oxide particles, the possibility that compositional changes had occurred in these two groups was investigated. As the biological material in the cell contains significant O and contributes slightly to the S signal, it is not straightforward to determine the compositions of the particles quantitatively. Therefore, relative S/Fe and O/Fe ratios in individual particles were determined by measuring the total intensity in selected (7 × 7 pixel) regions of the chemical maps, centered on the particles. The background O and S levels were set to zero on the basis of the respective intensities of these elements outside the cell. By using this method, 35 sulfide and 10 oxide particles were analyzed within the boxed area marked in Figure 4b.

Ratios of S/Fe and O/Fe measured from the Fe-sulfide particles are plotted in Figure 6a as a function of the distances of the magnetosomes from the cell-division plane. Although there is some scatter in the points, the S/Fe and O/Fe ratios clearly vary with increasing distance from the center of the dividing cell. Particles that are closer to the division plane generally have higher S/Fe and lower O/Fe ratios. We attribute the trend in these ratios in the sulfide particles to variable degrees of oxidation of greigite during sample storage. The chemical maps
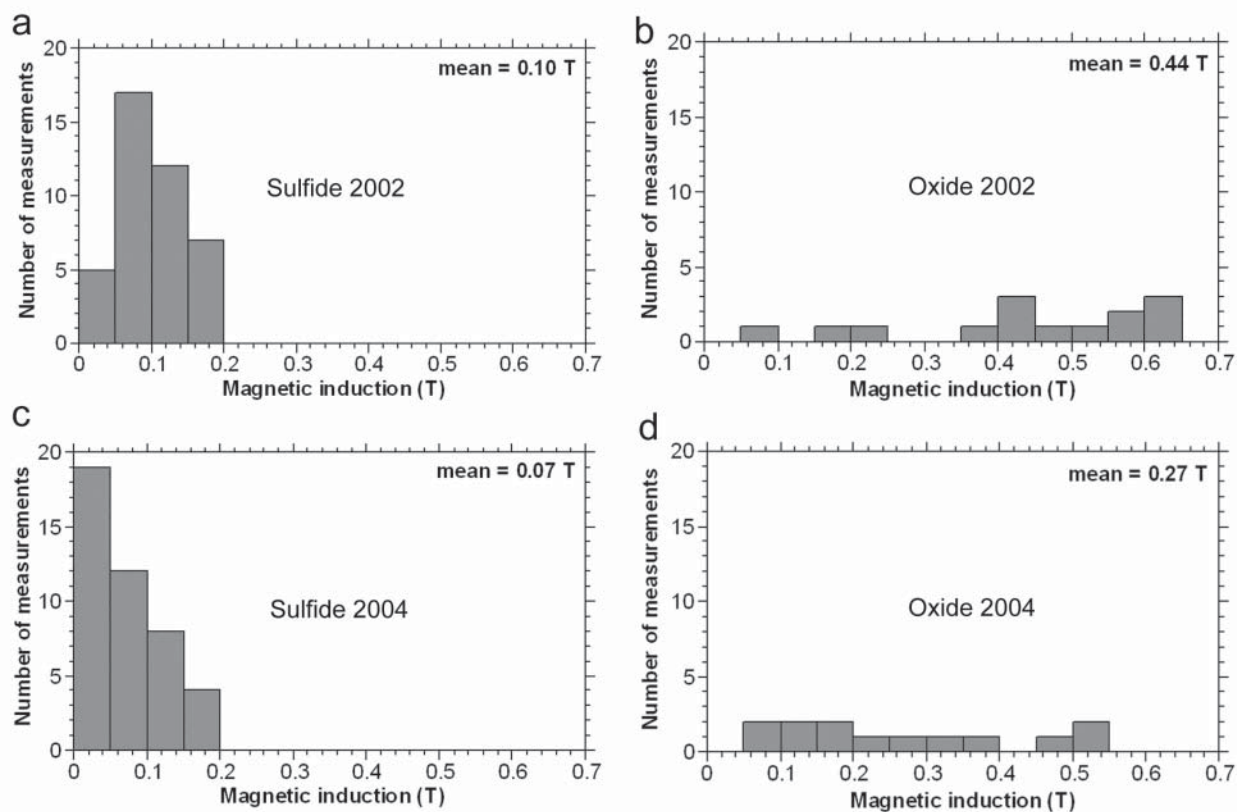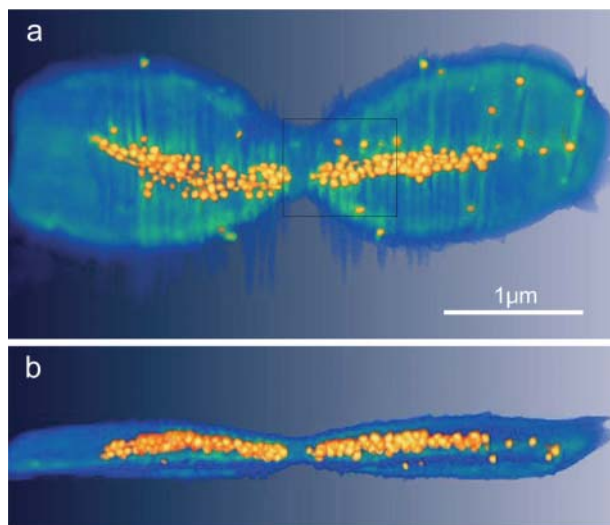

FIGURE 9. Histograms showing magnetic induction measured from individual particles using electron holography. The graphs are for particles from the dividing cell shown in Figure 4. (**a**) Sulfide particles measured in 2002; (**b**) oxide particles measured in 2002; (**c**) sulfide particles measured in 2004; (**d**) oxide particles measured in 2004. The magnetic induction values are consistent with the sulfide particles being greigite and the oxide particles being magnetite. Sulfide and oxide particles were identified on the basis of their compositions measured in 2004.
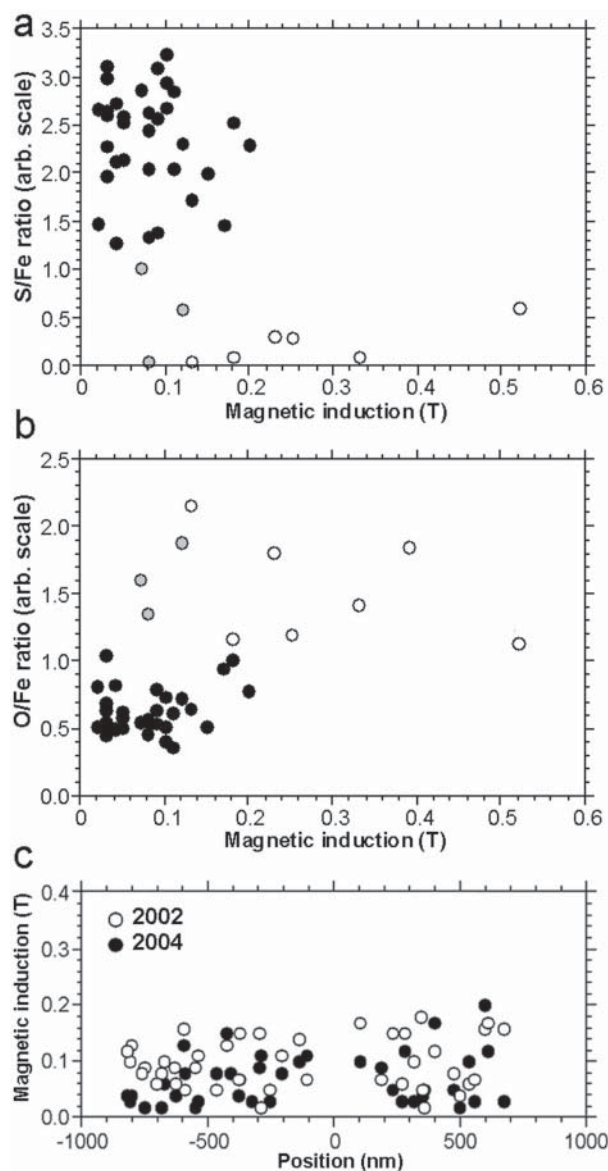
FIGURE 10. (**a**) S/Fe and (**b**) O/Fe ratios of particles from the boxed region in Figure 4b, plotted on an arbitrary scale as a function of their magnetic induction. All measurements were performed in 2004. Filled circles represent sulfide particles, and open and lightly shaded circles denote elongated rod-shaped and flake-like oxide particles, respectively. (**c**) Magnetic induction of sulfide particles from the same region, plotted as a function of their positions within the magnetosome chain. The origin on the horizontal axis corresponds to the cell division plane. Open and filled circles represent values that were measured in 2002 and 2004, respectively.

FIGURE 11. Two views of a three-dimensional tomographic reconstruction of the dividing cell in Figure 4, obtained from an ultra-high-tilt series of high-angle annular dark-field images. The magnetosomes are shown in yellow, whereas other cell materials are shown in blue. (**a**) and (**b**) show "top" and "side" views, respectively, of the dehydrated, flattened cell.
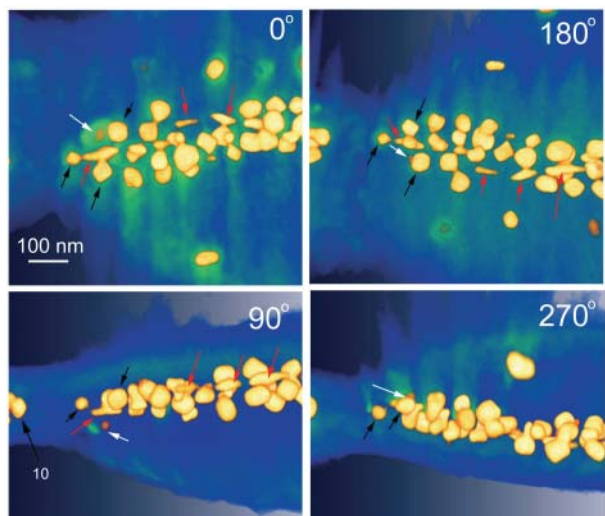
FIGURE 12. Higher-resolution tomographic reconstruction of the boxed region marked in Figure 11a, viewed from four different directions, which are indicated on the images. Black and white arrows mark the same crystals as in Figure 5. Red arrows indicate elongated, thin crystals.

Crystal structures and orientations measured from SAED patterns and HRTEM images

The structures of the magnetosomes that are numbered in Figures 3 and 4 were characterized using SAED patterns (acquired in 2002 and 2005) and HRTEM images (acquired in 2002). SAED patterns of crystals 1 to 15 are consistent with greigite. No reflections corresponding to mackinawite or to any other Fe-sulfide mineral appeared in the patterns. However, extended defects such as stacking faults and dislocations, as well as patchy con-

shown in Figure 5 reveal that the Fe-sulfide crystals are rimmed by an oxide layer. Compositional variations also are observed in the elongated and flake-like Fe-oxide particles, although the smaller number of crystals analyzed makes the identification of systematic changes difficult, and the variable S content of the cell material also contributes to the signal (Fig. 6b). The relationships between particle compositions and shapes are illustrated in the form of a shape-distribution diagram in Figure 6c.

trast, occur in HRTEM images (Fig. 7). Similar patchy contrast was observed in other sulfide-containing cells and attributed to the strain that results from the presence of defects (Pósfai et al. 1998a, 1998b). The defects were interpreted as resulting from a mackinawite to greigite solid-state conversion process. Other factors, including thickness variations, also may contribute to the uneven contrast.

Many greigite crystals in Figure 5 appear to be agglomerates of smaller grains, as if several nuclei had merged in a consistent crystallographic orientation during crystal growth. The resulting irregular shapes may contribute to the highly variable diffraction contrast observed in conventional bright-field images of the crystals. Smaller, thin crystal fragments appear to be attached to the surfaces of several crystals (Fig. 7a), contributing to their uneven thicknesses and, accordingly, to the contrast variation in bright-field images.

The crystallographic orientations of the greigite magnetosomes, with respect to one another, are as random as their morphologies. Whereas crystals in magnetite-producing bacteria often are elongated along [111], with an axis of elongation that is aligned parallel to the magnetosome chain (Simpson et al. 2005), the greigite crystals in the two cells that were examined here have highly variable orientations. No major crystallographic direction is preferred as the axis of elongation. The alignment of the crystals with respect to the chain axis also varies randomly, even though in a previous study some magnetosomes appeared to be aligned preferentially with [100] parallel to the chain (Pósfai et al. 1998b). Tables 1 and 2 (see page 1221) summarize the crystallographic, compositional, and magnetic features of individual magnetosomes in the cells shown in Figures 3 and 4, respectively, from which SAED patterns and HRTEM images were obtained. It is apparent from Tables 1 and 2 and Figure 6c that some of the greigite crystals are slightly elongated. However, their width/length ratios are nowhere smaller than 0.62, whereas the same ratio is typically between 0.2 and 0.4 for the highly elongated oxide particles.

Several Fe-sulfide magnetosomes have a faint halo around them in bright-field images (Fig. 5c). This halo is almost certainly of amorphous material, as it shows neither lattice fringes nor diffraction contrast on tilting. The positions of the halos coincide with the presence of O-rich shells around the crystals; such shells are marked using black arrows in the chemical map in Figure 5a. SAED patterns also were obtained in 2005, by which time many greigite magnetosomes had developed thick oxide shells. These patterns remain consistent with the greigite structure (Fig. 5c).

The only Fe-oxide particle from which SAED patterns were obtained is crystal 16 (Fig. 5). The patterns indicate that this crystal is either magnetite or maghemite, and its elongation axis is parallel to [100] (Fig. 5c).

Magnetic properties measured using electron holography

The magnetic induction in the specimen, measured using electron holography, is displayed conveniently in the form of contours formed from the magnetic contribution to the phase shift, as shown in Figures 3 and 4. Only the magnetic induction perpendicular to the electron beam direction is recorded in such maps. The maps are quantitative in the sense that the same amount of magnetic flux is enclosed between any two adjacent contours.

The magnetosome chain in the cell in Figure 3 contains magnetic phase contours that are generally parallel to the axis of the chain. However, there is considerable variation in the local directions of the contours within individual particles. The lower chain appears to be magnetized more uniformly than the upper chain, which comprises three short segments between which the contours either turn back on themselves or join those in the lower chain. The strength of the magnetic signal in the crystals apparently becomes progressively weaker toward the ends of the chains. Surprisingly, some crystals such as those at the ends and to one side of the chains have no contours inside them and thus appear to be non-magnetic. These crystals are marked in yellow in the inset to Figure 3.

Both halves of the magnetosome chain in the dividing cell also exhibit complicated magnetic contours (Fig. 4a). The multiple chain consists of several, approximately uniformly magnetized, linear segments of three or four magnetosomes. These segments, which are indicated using red lines in Figure 8a, are associated with bundles of contours whose direction may deviate from that of the chain axis. The contours in the elongated magnetosomes are generally parallel to the long axis of each crystal. Many magnetosomes that are marked in yellow in Figure 8b contain few (1–3) contours or none at all. Most crystals that appear to be non-magnetic are located away from the main axis of the mutiple chain.

The general direction of the magnetic induction measured in the multiple chain is similar in the maps recorded in 2002 and 2004. In each case, the magnetosomes are magnetized approximately parallel to the chain axis. However, the number of magnetic phase contours recorded across the entire chain is lower in 2004 (Fig. 4b) than in 2002 (Fig. 4a), indicating that the overall magnetization of the crystals has decreased over two years. This decrease is most notable on the left side of the chain, where the chemical map in Figure 4b also shows the most significant compositional changes, as indicated by the predominantly blue color. It appears that the partial conversion of Fe-sulfides into amorphous oxides has resulted in a net decrease in the magnetization of the individual crystals.

Quantitative measurements of the magnetic induction in individual magnetosomes were performed on the particles from which detailed compositional data were available (in the boxed area in Fig. 4b). To calculate the magnetic induction from the electron holographic phase images, the cross-sectional size of each particle, in a direction perpendicular to the contours, was determined. This size measurement was made from two HAADF images acquired at specimen tilt angles of +45° and –45° for each magnetosome. The induction was calculated on the assumption of infinite cylindrical particle shapes. The results reveal that the magnetic induction in the particles is related to their composition, phase, and morphology, as shown in Figure 9. Even though the distribution of measurements of magnetic induction is wide, the elongated oxide particles were clearly more strongly magnetic than the more equidimensional sulfide crystals, both in 2002 and in 2004.

The measured induction in the sulfide particles is approximately consistent with values expected from the literature for

greigite (~0.16 T) (Dunlop and Özdemir 1997). In contrast, the measurements for the elongated oxide particles are closer to those expected for either magnetite (0.60 T) or maghemite (0.48 T) (Dunlop and Özdemir 1997). Because several of the elongated particles showed induction values larger than 0.48 T in 2002, it is likely that they were originally magnetite.

Both the sulfide and the oxide particles were more weakly magnetic in 2004 than in 2002 (Fig. 9). Although artifacts of data processing cannot be excluded, the observed decrease in magnetization may result from the partial oxidation of both the sulfide and the oxide particles. It appears that chemical changes have resulted in a weaker magnetic induction, but the direction of the field in each particle has remained approximately the same (Fig. 4).

The relationship between composition and magnetic induction was studied further by plotting the measured S/Fe and O/Fe ratios (on an arbitrary scale) as a function of the magnetic induction, measured in 2004 (Figs. 10a and 10b). The points in these graphs are for the same particles for which compositions are shown in Figure 6. Sulfide and oxide particles are clearly distinct from each other in terms of both their morphology and their magnetic induction. Based on their morphology, Fe-oxide particles can be grouped into "elongated" and "flake-like" categories (Figs. 10a and 10b). The elongated particles are more strongly magnetic than the flake-like crystals, perhaps because a greater fraction of the volume of the flake-like particles had oxidized. Alternatively, their volumes may have been overestimated, resulting in an apparently lower magnetic induction.

The scatter in the measured magnetic induction values of the greigite particles is likely related to a lower probability that their magnetization directions are constrained to lie in the plane of the specimen. Measured induction values that are lower than 0.16 and 0.60 T for sulfide and oxide particles, respectively, may be explained by the presence of strong out-of-plane components of their magnetization, the effect of demagnetizing fields on the measurements, or both. Variations in the S/Fe and O/Fe ratios could also affect the magnetic induction of greigite particles. However, there is no clear relationship between the positions of sulfide magnetosomes relative to the division plane and their induction values (Fig. 10c), even though the compositions of greigite particles are observed to change according to their position in the cell (Fig. 6a).

Crystal morphologies, orientations, and positions measured using electron tomography

Figure 11 shows an electron tomographic reconstruction of the dividing cell, in which blue corresponds to the organic material and yellow to the magnetosomes. The green color inside and the blue spikes outside the cell are artifacts that arise primarily from the fact that images could not be acquired over the full tilt range of ±90°. Although the cell appears to be relatively intact in Figures 4 and 11a, the tomographic reconstruction shows that it is actually flat, presumably through the loss of most of the cell volume by dehydration (Fig. 11b).

Because relatively low-magnification HAADF images were used to obtain the reconstruction of the entire cell shown in Figure 11, the spatial resolution is insufficient to resolve the morphological details of the individual magnetosomes clearly.

Nevertheless, the images show that the multiple chains have a three-dimensional arrangement, as if they were inside a tube that runs parallel to the long axis of the cell. Because the cell is flattened in such a way that one side is concave, the original position of the multiple magnetosome chain relative to the cell wall cannot be measured. However, owing to the three-dimensional arrangement of the magnetosome chains, it is likely that at least some of the Fe-sulfide crystals may be close to the center of the cell, instead of being anchored to the cell wall as in some magnetite-bearing bacteria (Bazylinski and Frankel 2004). Several scattered crystals in the cell appear to be outside the primary "tube" of chains and to be independent of the chain configuration. Although the flattening of the cell during dehydration may have changed the original orientations of the crystals slightly, we do not believe that it caused the dispersal of magnetosomes from the chain structure.

A higher-spatial-resolution tomographic reconstruction, obtained from a –78° to +78° tilt series of higher-magnification HAADF images, is shown in Figure 12. This region corresponds to the boxed region in Figure 11a. The magnetosomes can now be seen to have highly irregular, variable morphologies. The tomographic reconstruction confirms that the Fe-oxide particles are either flake-like or have elongated, almost needle-like habits (marked using red arrows in Fig. 12). The morphologies of the elongated magnetosomes appear to highly constrain the direction of the magnetic induction to be parallel to their axes (Fig. 4a).

DISCUSSION

Conversion of magnetosomes

Previous studies have shown that Fe sulfide magnetosomes are initially non-magnetic mackinawite (FeS) and later convert to greigite (Pósfai et al. 1998a, 1998b). It is tempting to interpret the presence of weakly magnetic particles at the edges and the ends of the magnetosome chains (Figs. 4 and 8b) as being suggestive of the presence of unconverted mackinawite. However, SAED patterns and HRTEM images obtained from several of these sulfide magnetosomes are consistent with the crystal structure of greigite. As discussed above, these particles may appear to be weakly magnetic because they are magnetized largely out of the plane of the sample and therefore almost parallel to the electron beam direction. The weaker magnetization also may be related to demagnetizing fields, which should affect the particles closer to the ends of the chain more strongly than those in the center.

The cells were first studied several months after they were collected. As the mackinawite to greigite conversion was found to take place within about a week in samples that were stored in air (Pósfai et al. 1998b), any Fe-sulfides other than greigite are likely to have converted to greigite by the time of our studies. Therefore, the present magnetic data do not provide information about the mackinawite to greigite transition. However, the partial transformation of greigite to amorphous Fe-oxide in the dividing cell during sample storage is well documented in the present study and is consistent with the magnetic and the compositional data. Because the samples were stored in a vial and exposed to the atmosphere, O_2 could enter the cells and react with the magnetosomes. Having been collected in the spring of 2002, many sulfide magnetosomes already had oxide rims when
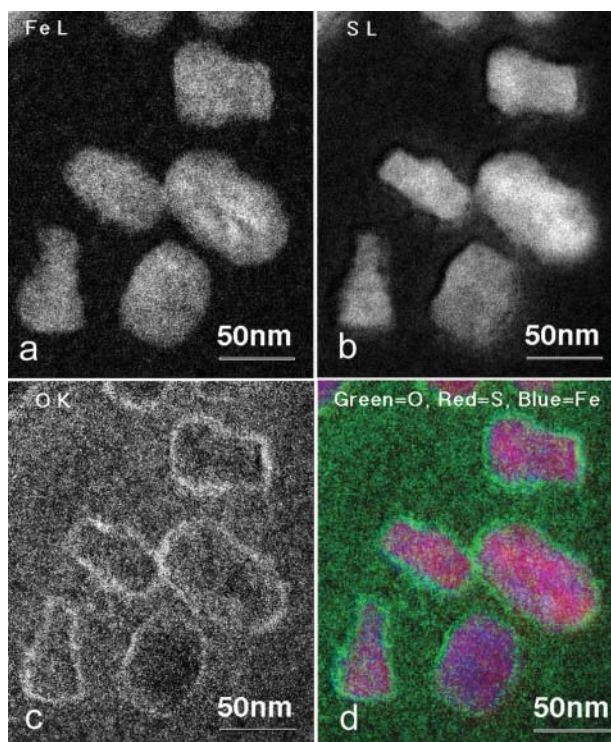
FIGURE 13. Three-window, background-subtracted chemical maps of Fe-sulfide magnetosomes obtained from a cell of a multicellular magnetotactic prokaryote. The crystals have distinct shells of amorphous Fe-oxide. The chemical element and the electron energy-loss edge that was used for the maps are indicated in each image.

they were first examined in the fall of 2002. By the time they were reexamined in 2004, most of the greigite magnetosomes had developed distinct oxide shells (Figs. 5 and 6). As indicated in Figure 6a, the degree of greigite oxidation is not uniform along the cell; the magnetosomes that are further laterally from the center of the cell appear to be more oxidized. This trend may reflect pre-existing compositional differences among the greigite magnetosomes, although the possibility that this observation results from variations in the O content of the organic cell materials cannot be ruled out. The process by which S is released from the magnetosomes by oxidation is also unclear; presumably it diffuses as SO_2 into the cell.

The conversion of sulfide magnetosomes in rod-shaped cells over time is not unique. We observed similar compositional features in cells from the multicellular magnetotactic prokaryote, an organism that forms cell aggregates that move as single units (Rodgers et al. 1990; Lins and Farina 1999; Keim et al. 2004a, 2004b). Chemical maps obtained from a sample two years after it was collected indicate that the Fe-sulfide magnetosomes have Fe-oxide surface shells (Fig. 13). Similar shells on greigite magnetosomes were also noticed by Farina et al. (1992).

Because the oxide shells are amorphous, they reduce the magnetic moment of the original greigite crystals. Such a reduction in magnetic induction over two years is apparent in Figure 9. The decrease in the magnetization of greigite over time has been considered in paleomagnetic studies (Dekkers et al.

2000). Greigite did not remain stable either in sediments or in rock samples that were stored for longer periods (Snowball and Thompson 1990). It is likely that, under oxic conditions, greigite particles in sediments will develop oxide shells similar to those observed on the magnetosomes. It remains to be determined whether the conversion of greigite magnetosomes continues beyond the formation of oxide shells and the greigite crystals eventually completely turn into amorphous Fe-oxide. If at least part of the original sulfide is preserved, then magnetosome-sized greigite crystals can be used as biomarkers both in soil (Stanjek et al. 1994) and in sedimentary rock samples (Pósfai et al. 2001), and they may be useful as biomarkers in archaeological studies (Linford et al. 2005). The distinctive shapes of crystal size distributions could be used in such studies to identify magnetofossils (Pósfai et al. 2001). Because several generations of greigite can form diagenetically in sedimentary rocks and each of these contributes to the total magnetization, complicating magnetostratigraphic interpretation (Rowan and Roberts 2006), it is important to know which, if any, of the greigite particles were deposited as magnetofossils.

Oxidation also affects the magnetite magnetosomes that occur with greigite in the dividing cell shown in Figure 4. The magnetic induction measured in the Fe-oxide particles decreased between 2002 and 2004 (Fig. 9), presumably owing to the maghemitization of the original magnetite partices. Such transformations have been inferred from bulk magnetic measurements of magnetite crystals originating from magnetite-producing magnetotactic bacteria (Moskowitz 1995; Carter-Stiglitz et al. 2004; Pan et al. 2005).

Relationship between composition, morphology, crystallographic orientation, and magnetization

Although all the sulfide magnetosomes were found to be greigite, their measured magnetic induction appears to vary significantly, presumably as a result of variations in their morphology and orientation. Compositional variations may also slightly affect the magnetic induction. The greigite crystals are either slightly elongated or almost equidimensional (see Fig. 6c and the shape factor columns in Tables 1 and 2). In general, the more elongated crystals appear to be more strongly magnetic, particularly if the elongation and chain axes are parallel to one another. However, the long axes of many crystals are not parallel to the chain axis, particularly in the outer regions of the multiple chain. Such crystals typically either appear to be non-magnetic, or their induction lines are parallel to the elongation of the crystal rather than to the chain axis (crystals 2, 4, 5, 9, and 12 in Tables 1 and 2). The apparently non-magnetic crystals have elongation axes that do not lie parallel to the chain, are probably magnetized largely out of the plane of the flat cell and thus contribute little to the in-plane magnetic signal recorded using electron holography. In general, the random crystallographic orientations of the greigite particles do not appear to affect their magnetic induction. Thus, the shape anisotropy of most greigite magnetosomes appears to be the most important factor that controls their magnetization direction (unless they are very closely spaced), followed by interparticle interactions, whereas magnetocrystalline anisotropy is the least important.

Based on theoretical considerations, Diaz-Ricci and Kirsch-

vink (1992) calculated the size- and shape-dependent magnetic properties of greigite and suggested that the sizes of the greigite magnetosomes place them at the boundary of the superparamagnetic and single magnetic domain size range. They also found that the crystal shape significantly affects the magnetic properties of isolated greigite crystals. Whereas ~70 nm particles with prismatic habits were calculated to be single domains, spheroidal particles of the same size were superparamagnetic. Our results indicate that equidimensional greigite particles as small as ~40 nm can be single magnetic domains. Either the boundary between the superparamagnetic and the single domain ranges is at a lower value than calculated by Diaz-Ricci and Kirschvink (1992) or magnetic interactions between the chain-bound particles constrain the magnetization direction to lie in a particular direction (i.e., thermal fluctuations are overcome).

A striking contrast exists between the magnetic behavior of the greigite magnetosomes and that of magnetite magnetosomes in other types of bacteria. In all magnetite-producing strains that have been studied using electron holography (Dunin-Borkowski et al. 1998; 2001; McCartney et al. 2001; Simpson et al. 2005), the magnetite crystals are organized in relatively straight chains, with each particle aligned such that [111] is parallel to the chain axis, resulting in a fairly uniform magnetic induction along the chain in terms of both magnitude and direction. The strict biological control that results in the presence of uniform morphologies, sizes and orientations of magnetite magnetosomes appears to be weaker in greigite-producing bacteria, perhaps as a result of a different biomineralization process. The random shapes and orientations of the greigite magnetosomes result in a variable, winding magnetic field along the chain. Nevertheless, the chain contains many magnetosomes that collectively produce an overall magnetic moment that is parallel to the long axis of the cell and enables it to migrate along magnetic field lines.

The dividing cell in Figure 4 contains both greigite and Fe-oxide magnetosomes. Magnetite was found together with greigite in rod-shaped bacteria by Bazylinski et al. (1995), and amorphous Fe-oxide particles have been described in magnetotactic multicellular aggregates (Lins and Farina 2001). The Fe-oxide magnetosomes that are described in the present study are all magnetic and therefore must also be crystalline. They are typically highly elongated, with an elongation axis parallel to [100]. Similarly elongated biogenic magnetite particles were found by Vali and Kirschvink (1989). Whereas SAED patterns obtained from one of these elongated oxides are consistent with both magnetite and maghemite, the magnetic data suggest that the particles are magnetite. The elongated shapes constrain the direction of magnetic induction, as seen from the dense and parallel contour lines in the particles marked by red arrows in Figure 4a. Because these particles are aligned with their long axes parallel to the chain axis, they contribute significantly (~30%) to the total magnetic moment of the cell.

In addition to the magnetosomes in the multiple chains, some greigite crystals are apparently scattered in the cytoplasm. Their presence raises the possibility that the magnetosomes form at random locations in the cell and then assemble into chains. A similar mechanism operates under special conditions in *Magnetospirillum gryphiswaldense*, a magnetite-producing bacterium (Scheffel et al. 2005). Some Fe-free, S- and O-bearing particles

also occur in both cells (marked by white arrows in Figs. 2d and 4a). These particles appear to be near the cell wall and are presumably unrelated to magnetosome formation.

The total magnetic moment of a cell also can be determined from electron holography. By using the method described by Dunin-Borkowski et al. (1998), we measured a magnetic moment of 9.0×10^{-16} Am^2 for the cell in Figure 3. Almost exactly the same value (9.5×10^{-16} Am^2) was calculated by Heywood et al. (1990) for a greigite-bearing cell on the basis of literature data and particle volumes.

The dividing cell in Figure 4 had a magnetic moment of 1.8×10^{-15} Am^2 in 2002, exactly double that of the single cell (Fig. 3). This is the first definitive evidence that daughter cells inherit parental magnetosomes and that the two daughter cells are magnetotactically viable (i.e., $MB/k_BT \geq 10$, where M is the cellular magnetic moment, B is the geomagnetic field, k_B is Boltzmann's constant, and T is temperature), as soon as they separate from each other. For comparison, magnetic moments of magnetite-producing strains *Magnetospirillum magnetotacticum* MS-1 and MV-1, were measured to be 5×10^{-16} and 7×10^{-16} Am^2, respectively (Dunin-Borkowski et al. 1998). As a result of oxidation of the magnetosomes during specimen storage, the magnetic moment of the dividing cell had decreased to 1.4×10^{-15} Am^2 by 2004.

The presence of both magnetite and greigite magnetosomes in the same cell raises the question of whether the cell would be sufficiently magnetic for magnetotaxis if it contained sulfide magnetosomes only. The separate contributions of oxide and sulfide particles to the total magnetic moment were calculated for the chain fragment within the boxed area in Figure 4b. We multiplied the magnetic phase shift across each particle by the particle length along the induction direction and by h/2πe, and then summed the moments of individual particles. The magnetic moments of oxide and sulfide particles are 1.4×10^{-16} and 3.5×10^{-16} Am^2, respectively. Thus, in this part of the magnetosome chain the contribution of oxide particles to the total magnetic moment is ~30%. Extrapolating the measured ratio of magnetic contributions of magnetite and greigite magnetosomes to the entire cell, in 2002 the magnetic moment solely attributable to the greigite magnetosomes was ~6.3×10^{-16} Am^2 in each daughter cell, resulting in $MB/k_BT \approx 7.5$. The daughter cells would therefore migrate parallel to the geomagnetic field at more than 80% of their forward speed (Frankel 1984) even without the magnetite magnetosomes.

Except for the evidence that greigite magnetosomes develop from nonmagnetic Fe-sulfide precursors (Pósfai et al. 1998b), the biomineralization process in greigite-bearing bacteria is virtually unknown. Magnetite biomineralization in *Magnetospirillum gryphiswaldense* is thought to be associated with the gene products of a 130 kilobase genomic region that comprises a "magnetosome island" (Ullrich et al. 2005). However, the roles of many of the gene products are as yet unknown. Nevertheless, a scheme for the biomineralization process has been proposed (Scheffel et al. 2006; Komeili et al. 2006). The magnetosome membrane vesicles, which envelop the mineral crystals, form prior to initiation of crystal nucleation by invagination of the cytoplasmic membrane (CM) and remain attached to the CM during growth of the crystals. The magnetosomes also are associated with a

system of actin-like filaments that are presumably involved in the organization of the magnetosomes in chains. The filaments lie close to the CM, allowing the magnetosome vesicles to be associated simultaneously with the filaments and the CM. The process of magnetosome formation in the Fe-sulfide-bearing magnetotactic rods might be similar to that in magnetite-bearing bacteria, with magnetite-forming vesicles and Fe-sulfide-forming vesicles co-organized by filaments (Bazylinski et al. 1995).

The function of magnetotaxis in these greigite-bearing cells is enigmatic because they inhabit sulfidic sediments and waters below the oxic-anoxic transition zone (OATZ). In such environments, strong vertical oxygen concentration gradients are absent. Thus, the utility of magnetotaxis cannot be magnetically assisted aerotaxis as in many magnetite-bearing bacteria (Frankel et al. 1997). Several authors (e.g., Simmons et al. 2004) have suggested that internal Fe minerals might be connected to metabolic or detoxification functions of the cell. Nevertheless, the uniform magnetic moments of the various cells that were measured in this and previous studies (Dunin-Borkowski et al. 1998, 2001) suggest that the development of magnetosome chains is optimized to provide the cell with a magnetic moment that enables it to navigate magnetically. Even the rod-shaped, greigite-bearing cells described here seem to produce magnetosomes with the primary function of enabling magnetotaxis. Such microorganisms may use magnetically assisted chemotaxis to respond to as yet unidentified environmental stimuli.

In the present study, we have used several advanced TEM techniques to characterize iron sulfide magnetosomes inside the cells of magnetotactic bacteria. By using a combination of SAED, HRTEM, and electron tomography, the shapes and the crystallographic orientations of the magnetosomes were determined, with respect to both the magnetosome chain axis and the elongation directions of the particles. We also obtained magnetosome compositions using energy-filtered imaging. These data were correlated with the magnetic induction of the magnetosomes, measured using electron holography. The combined data set revealed that the direction of the magnetic field in individual greigite magnetosomes is dominated by shape anisotropy and by interparticle interactions. The orientations and the relative positions of the greigite magnetosomes appear to vary widely in the magnetosome chain, resulting in a lower efficiency in generating a magnetic moment than in magnetite-producing bacteria that contain well-ordered magnetosome chains. However, the large number of greigite magnetosomes in the chain, as well as the presence of highly elongated magnetite particles among the iron sulfides, results in a magnetic moment that is sufficient for magnetotaxis.

REFERENCES CITED

Bazylinski, D.A. and Frankel, R.B. (2004) Magnetosome formation in prokaryotes. Nature Reviews Microbiology, 2, 217–230.

Bazylinski, D.A., Frankel, R.B., Garratt-Reed, A.J., and Mann, S. (1990) Biomineralization of iron sulfides in magnetotactic bacteria from sulfidic environments. In R.B. Frankel, and R.P. Blakemore, Eds. Iron biominerals, p. 239–255. Plenum

Press, New York.

Bazylinski, D.A., Heywood, B.R., Mann, S., and Frankel, R.B. (1993) Fe_3O_4 and Fe_3S_4 in a bacterium. Nature, 366, 218.

Bazylinski, D.A., Frankel, R.B., Heywood, B.R., Mann, S., King, J.W., Donaghay, P.L., and Hanson, A.K. (1995) Controlled biomineralization of magnetite (Fe_3O_4) and greigite (Fe_3S_4) in a magnetotactic bacterium. Applied and Environmental Microbiology, 61, 3232–3239.

Buseck, P.R., Dunin-Borkowski, R.E., Devouard, B., Frankel, R.B., McCartney, M.R., Midgley, P.A., Pósfai, M., and Weyland, M. (2001) Magnetite morphology and life on Mars. Proceedings of the National Academy of Sciences of the United States of America, 98, 13490–13495.

Carter-Stiglitz, B., Moskowitz, B.M., and Jackson, M. (2004) More on the low-temperature magnetism of stable single domain magnetite: Reversibility and non-stoichiometry. Geophysical Research Letters, 31, L06606, doi:10.1029/2003GL019155.

Chen, X., Zhang, X., Wan, J., Wang, Z., and Qian, Y. (2005) Selective fabrication of metastable greigite (Fe_3S_4) nanocrystallites and its magnetic properties through a simple solution-based route. Chemical Physics Letters, 403, 396–399.

Dekkers, M.J., Passier, H.F., and Schoonen, M.A.A. (2000) Magnetic properties of hydrothermally synthesized greigite (Fe_3S_4) - II. High- and low-temperature characteristics. Geophysical Journal International, 141, 809–819.

Diaz-Ricci, J.C. and Kirschvink, J.L. (1992) Magnetic domain state and coercivity predictions for biogenic greigite (Fe_3S_4): A comparison of theory with magnetosome observations. Journal of Geophysical Research, 97, 17309–17315.

Diaz-Ricci, J.C., J., W.B., Kirschvink, J.L., and Hoffman, M.R. (1991) Alteration of the magnetic properties of Aquaspirillum magnetotacticum by a pulse magnetization technique. Applied and Environmental Microbiology, 57, 3248–3254.

Dunin-Borkowski, R.E., McCartney, M.R., Frankel, R.B., Bazylinski, D.A., Pósfai, M., and Buseck, P.R. (1998) Magnetic microstructure of magnetotactic bacteria by electron holography. Science, 282, 1868–1870.

Dunin-Borkowski, R.E., McCartney, M.R., Pósfai, M., Frankel, R.B., Bazylinski, D.A., and Buseck, P.R. (2001) Off-axis electron holography of magnetotactic bacteria: magnetic microstructure of strains MV-1 and MS-1. European Journal of Mineralogy, 13, 671–684.

Dunin-Borkowski, R.E., McCartney, M.R., and Smith, D.J. (2004) Electron holography of nanostructured materials. In H.S. Nalwa, Ed. Encyclopedia of Nanoscience and Nanotechnology, 3, 41–100. American Scientific Publishers.

Dunlop, D.J. and Özdemir, Ö. (1997) Rock magnetism: Fundamentals and frontiers. Cambridge University Press, Cambridge.

Egerton, R.F. (1986) Electron energy-loss spectroscopy in the electron microscope. 410 p. Plenum, New York.

Farina, M., Esquivel, D.M.S., and Lins de Barros, H.G.P. (1990) Magnetic iron-sulphur crystals from a magnetotactic microorganism. Nature, 343, 256–258.

Farina, M., Lins, U., Lins de Barros, H.G.P., and Broderick, R. (1992) Multiple mineral precipitations inside magnetotactic microorganisms. Proceedings of the 50th Annual Meeting of the Electron Microscopy Society of America, 878–879.

Frankel, R.B. (1984) Magnetic guidance of organisms. Annual Reviews in Biophysics and Bioengineering, 13, 85–103.

Frankel, R.B., Bazylinski, D.A., Johnson, M.S., and Taylor, B.L. (1997) Magneto-aerotaxis in marine coccoid bacteria. Biophysical Journal, 73, 994–1000.

Heywood, B.R., Bazylinski, D.A., Garratt-Reed, A., Mann, S., and Frankel, R.B. (1990) Controlled biosynthesis of greigite (Fe_3S_4) in magnetotactic bacteria. Naturwissenschaften, 77, 536–538.

Heywood, B.R., Mann, S., and Frankel, R.B. (1991) Structure, morphology and growth of biogenic greigite (Fe_3S_4). Materials Research Society Symposium, Proceedings, 218, 93–108.

Hoffmann, V. (1992) Greigite (Fe_3S_4): magnetic properties and first domain observations. Physics of the Earth and Planetary Interiors, 70, 288–301.

Keim, C.N., Abreu, F., Lins, U., Lins de Barros, H.G.P., and Farina, M. (2004a) Cell organization and ultrastructure of a magnetotactic multicellular organism. Journal of Structural Biology, 145, 254–262.

Keim, C.N., Martins, J.L., Abreu, F., Rosado, A.S., Lins de Barros, H.G.P., Borojevic, R., Lins, U., and Farina, M. (2004b) Multicellular life cycle of magnetotactic prokaryotes. FEMS Microbiology Letters, 240, 203–208.

Komeili, A., Li, Z., Newman, D.K., and Jensen, G.J. (2006) Magnetosomes are cell membrane invaginations organized by the actin-like protein MamK. Science, 311, 242–245.

Linford, N., Linford, P., and Platzman, E. (2005) Dating environmental change using magnetic bacteria in archaeological soils from the upper Thames Valley, UK. Journal of Archaeological Science, 32, 1037–1043.

Lins, U. and Farina, M. (1999) Organization of cells in magnetotactic multicellular aggregates. Microbiological Research, 154, 9–13.

——— (2001) Amorphous mineral phases in magnetotactic multicellular aggregates. Archives of Microbiology, 176, 323–328.

Mann, S., Sparks, N.H.C., Frankel, R.B., Bazylinski, D.A., and Jannasch, H.W. (1990) Biomineralization of ferrimagnetic greigite (Fe_3S_4) and iron pyrite

(FeS$_2$) in a magnetotactic bacterium. Nature, 343, 258–261.

McCartney, M.R., Lins, U., Farina, M., Buseck, P.R., and Frankel, R.B. (2001) Magnetic microstructure of bacterial magnetite by electron holography. European Journal of Mineralogy, 13, 685–689.

Midgley, P.A., Weyland, M., Thomas, J.M., and Johnson, B.F.G. (2001) Z-contrast tomography: A technique in 3-dimensional nanostructural analysis based on Rutherford scattering. Chemical Communications, 10, 907–908.

Moskowitz, B.M. (1995) Biomineralization of magnetic minerals. Reviews in Geophysics Supplementum, 123–128.

Moskowitz, B.M., Frankel, R.B., and Bazylinski, D.A. (1993) Rock magnetic criteria for the detection of biogenic magnetite. Earth and Planetary Science Letters, 120, 283–300.

Pan, Y., Petersen, N., Winklhofer, M., Davila, A.F., Liu, Q., Frederichs, T., Hanzlik, M., and Zhu, R. (2005) Rock magnetic properties of uncultured magnetotactic bacteria. Earth and Planetary Science Letters, 237, 311–325.

Peters, C. and Dekkers, M.J. (2003) Selected room temperature magnetic parameters as a function of mineralogy, concentration and grain size. Physics and Chemistry of the Earth, 28, 659–667.

Pósfai, M., Buseck, P.R., Bazylinski, D.A., and Frankel, R.B. (1998a) Iron sulfides from magnetotactic bacteria: Structure, composition, and phase transitions. American Mineralogist, 83, 1469–1481.

——— (1998b) Reaction sequence of iron sulfide minerals in bacteria and their use as biomarkers. Science, 280, 880–883.

Pósfai, M., Cziner, K., Márton, E., Márton, P., Buseck, P.R., Frankel, R.B., and Bazylinski, D.A. (2001) Crystal-size distributions and possible biogenic origin of Fe sulfides. European Journal of Mineralogy, 13, 691–703.

Proksch, R., Schäffer, T.E., Moskowitz, B.M., Dahlberg, E.D., Bazylinski, D.A., and Frankel, R.B. (1995) Magnetic force microscopy of the submicron magnetic assembly in a magnetotactic bacterium. Applied Physics Letters, 66, 2582–2584.

Roberts, A.P. (1995) Magnetic properties of sedimentary greigite (Fe$_3$S$_4$). Earth and Planetary Science Letters, 134, 227–236.

Rodgers, F.G., Blakemore, R.P., Blakemore, N.A., Frankel, R.B., Bazylinski, D.A., Maratea, D., and Rodgers, C. (1990) Intercellular structure in a many-celled magnetotactic prokaryote. Archives of Microbiology, 154, 18–22.

Rowan, C.J., and Roberts, A.P. (2006) Magnetite dissolution, diachronous greigite formation, and secondary magnetizations from pyrite oxidation: Unravelling complex magnetizations in Neogene marine sediments from New Zealand.

Earth and Planetary Science Letters, 241, 119–137.

Scheffel, A., Gruska, M., Faivre, D., Linaroudis, A., Plitzko, J.M., and Schüler, D. (2006) An acidic protein aligns magnetosomes along a filamentous structure in magnetotactic bacteria. Nature, 440, 110–114.

Simmons, S.L., Sievert, S.M., Frankel, R.B., Bazylinski, D.A., and Edwards, K.J. (2004) Spatiotemporal distribution of marine magnetotactic bacteria in a seasonally stratified coastal salt pond. Applied and Environmental Microbiology, 70, 6230–6239.

Simpson, E.T., Kasama, T., Pósfai, M., Buseck, P.R., Harrison, R.J., and Dunin-Borkowski, R.E. (2005) Magnetic induction mapping of magnetite chains in magnetotactic bacteria at room temperature and close to the Verwey transition using electron holography. Journal of Physics: Conference Series, 17, 108–121.

Snowball, I.F., and Thompson, R. (1990) A stable remanence in Holocene sediments. Journal of Geophysical Research, 95, 4471–4479.

Stanjek, H., Fassbinder, J.W.E., Vali, H., Wägele, H., and Graf, W. (1994) Evidence of biogenic greigite (ferrimagnetic Fe$_3$S$_4$) in soil. European Journal of Soil Science, 45, 97–103.

Ullrich S., Kube, M., Schubbe, S., Reinhardt, R., and Schuler, D. (2005) A hypervariable 130-kilobase genomic region of Magnetospirillum gryphiswaldense comprises a magnetosome island which undergoes frequent rearrangements during stationary growth. Journal of Bacteriology, 187, 7176–7184.

Vali, H., and Kirschvink, J.L. (1989) Magnetofossil dissolution in a palaeomagnetically unstable deep-sea sediment. Nature, 339, 203–206.

van Poppel, L.H., Friedrich, H., Spinsby, J., Chung, S.H., Seinfeld, J.H., and Buseck, P.R. (2005) Electron tomography of nanoparticle clusters: Implications for atmospheric lifetimes and radiative forcing of soot. Geophysical Research Letters, 32, L24811, 10.1029/2005GL024461.

Weiss, B.P., Kim, S.S., Kirschvink, J.L., Kopp, R.E., Sankaran, M., Kobayashi, A., and Komeili, A. (2004) Magnetic tests for magnetosome chains in Martian meteorite ALH84001. Proceedings of the National Academy of Sciences of the United States of America, 101, 8281–8284.